Elastic Tubes: Modeling Elastic Deformation of Hollow Tubes

H. Li[1], W. K. Leow[1] and I.-S. Chiu[2]

[1]Department of Computer Science, National University of Singapore, Singapore
[2]Department of Surgery, National Taiwan University Hospital, Taipei, Taiwan

Abstract
The Cosserat theory of elastic rods has been used in a wide range of application domains to model and simulate the elastic deformation of thin rods. It is physically accurate and its implementations are efficient for interactive simulation. However, one requirement of using Cosserat rod theory is that the tubular object must have rigid cross-sections that are small compared to its length. This requirement make it difficult for the approach to model elastic deformation of rods with large, non-rigid cross-sections that can change shape during rod deformation, in particular, hollow tubes. Our approach achieves this task using a hybrid model that binds a mesh elastically to a reference Cosserat rod. The mesh represents the surface of the hollow tube while the reference rod models bending, twisting, shearing and stretching of the tube. The cross-sections of the tube may take on any arbitrary shape. The binding is established by a mapping between mesh vertices and the rod's directors. Deformation of the elastic tube is accomplished in two phases. First, the reference rod is deformed according to Cosserat theory. Next, the mesh is deformed using Laplacian deformation according to its mapping to the rod and its surface elastic energy. This hybrid approach allows the tube to deform in a physically correct manner in relation to the bending, twisting, shearing, and stretching of the reference rod. It also allows the surface to deform realistically and efficiently according to surface elastic energy and the shape of the reference rod. In this way, the deformation of elastic hollow tubes with large, non-rigid cross-sections can be simulated accurately and efficiently.

Keywords: physics-based modeling, elastic tubes, Cosserat rod theory, Laplacian deformation

ACM CCS: I.3.5 [Computer Graphics]: Computational Geometry and Object Modeling

1. Introduction

Modeling of elastic tubular objects has been an active research area in recent years. Its application domains range from computer graphics and animation [BWR*08, BAC*06, ST07, ST08], computer aided design [GS07, TGAB08], mechanical engineering [GB06, LPY04, LCW04], DNA simulation [HMM03, GPL05], to surgical simulation [Pai02, CDL*05, LCDN06]. General physics-based deformable models such as 3D finite elements (FEM) and thin shell models can be applied to the modeling of thin rods and/or hollow tubes [NMK*05, TPBF87]. However, they are in general computationally expensive. Moreover, they do not explicitly model global bending and twisting, which are important characteristics of tubular objects.

In contrast, the Cosserat theory [Ant95, Rub00] has been developed to elegantly model bending and twisting, as well as shearing and stretching, of elastic rods. It represents a 3D tubular object using a 1D centerline and orthonormal directors associated with the centerline (Figure 2). Due to its physical accuracy and computational efficiency, it has been applied to a wide range of application domains including the simulation of surgical threads and catheters [Pai02, CDL*05, LCDN06], hair strands [BAQ*05, BAC*06], ropes and knots [ST07, ST08], cables [GS07], DNA [HMM03, GPL05], and scoliotic spine [LLHH09]. Cosserat rod theory makes the assumption that the rod has rigid cross-sections that are small compared to its length. Thus, it is not suitable for modeling elastic deformation of hollow tubes with large, non-rigid cross-sections.

To simulate hollow tubes with deformable cross-sections, Gould and Burton [GB06] presented a model that uses a sequence of Cosserat rings (rods whose two ends are joined) to represent the tube's cross-sections, and assembles the cross-sectional rings to form the tube. This approach is physically accurate. However, the model is very complex and computationally very expensive.

In this paper, we propose an efficient approach for simulating hollow tubes with large and deformable cross-sections. Our approach uses a hybrid model that binds a surface mesh model elastically to a reference Cosserat rod. The mesh model represents the surface of the hollow tube while the reference rod models global bending, twisting, shearing and stretching of the tube. The cross-sections of the tube may take on any arbitrary shape. Binding between the mesh and the rod is established by a mapping between mesh vertices and the rod's directors.

Our hybrid model deforms the surface mesh according to Laplacian deformation method [BS08, MYF06, Sor05], which is a computationally efficient approximation of thin shell model. Like thin shell model, it computes the mesh configuration that minimizes local surface bending and stretching. However, local surface bending is modeled using Laplacians (i.e., linear approximation of curvature normals), which are rotation-variant. Masuda et al. [MYF06] proposed a method to compute rotation-invariant Laplacians by approximating the rotations of the normals at the mesh vertices. In our model, rotation-invariance is achieved by measuring the Laplacians with respect to the directors of the reference rod, which are intrinsic properties of the rod. This is a more natural approach to achieving rotation invariance of Laplacian for tubular objects. Therefore, the reference Cosserat rod serves the important roles of modeling global bending, twisting, shearing, and stretching of the tube, as well as providing reference frames (i.e., directors) for achieving rotation-invariant Laplacian deformation. Explicit modeling of bending and twisting also allows these properties to be easily visualized, if necessary.

Our method deforms an elastic tube model in two phases. First, the reference rod is deformed according to Cosserat theory and user-specified boundary conditions. Next, the mesh is deformed using Laplacian deformation according to its mapping to the rod and its surface elastic energy. This hybrid approach allows the tube to deform in a physically correct manner in relation to the bending, twisting, shearing, and stretching of the reference rod. It also allows the surface to deform realistically and efficiently according to surface elastic energy and the shape of the reference rod. In this way, the deformation of elastic hollow tubes with large, non-rigid cross-sections can be simulated accurately and efficiently. Compared to existing work, we apply Cosserat rod theory to model all the strain variables of a rod, namely bending, twisting, shearing and stretching. In addition, direction is represented using Rodrigue's rotation
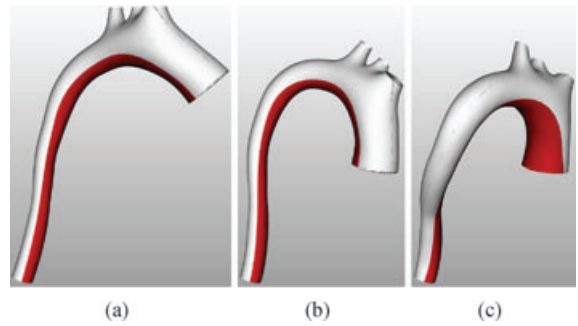
Figure 1: *Manipulation of aorta model. (a) Initial configuration. The lower end is fixed both in position and orientation. The other end is displaced (b) and then intentionally rotated, causing twisting of the aorta (c) for comparison.*

formula which has a minimum degree of freedom and is constraint-free.

Compared to FEM and thin shell model, our hybrid model trades physical correctness of surface modeling for computational efficiency. Nevertheless, the hybrid model can still deform in a physically realistic manner. Experimental tests (Section 6) show that the deformation of the hybrid model resembles those of real tubular objects.

Our target application is to model the deformation of great arteries (i.e., aorta and pulmonary trunk) in a *predictive* cardiac surgery simulation and planning system [LLQC09] (Figure 1). The system allows a surgeon to explore various surgical options by providing minimum amounts of user inputs. For instance, if the surgeon wants to join a blood vessel to another, he only needs to specify the joining ends of the two vessels. The system will efficiently predict the best configurations of the blood vessels, which have minimum deformation in terms of stretching, bending and twisting, to achieve the join. In this application, real-time response is not crucial but the deformation has to be sufficiently fast and accurate in order to allow the surgeon to efficiently explore various surgical options to determine the best ones. Furthermore, dynamic deformation of the blood vessels in response to interaction with surgical tools is not necessary as well.

In general, our hybrid model can be formulated to bind any surface model to the Cosserat rod. This general formulation will be presented in a continuous coordinate system (Section 3). In practice, for convenience and computational efficiency, the hybrid model is constructed from a triangular mesh that represents the tube's surface (Section 4), and is deformed based on the discrete elastic energy of the Cosserat rod and the surface mesh (Section 5). Experimental tests (Section 6) show that the simulation results are realistic. Before presenting the details of our hybrid model, let us first discuss existing related work.

2. Related Work

There are several models of elastic rods that are not based on Cosserat theory. Theetten et al. [TGAB08] presented a considerably accurate model for cable positioning simulation. The model expresses stretching, bending, and torsion energies in continuous form. In addition, it also accounts for the plasticity of material, which can result in irreversible deformation. The numerical scheme for simulating deformation can switch between dynamic and quasistatic modes to balance between animation accuracy and computational efficiency [TGDM07]. Bergou et al. [BWR*08] presented an elastic rod model for computer animation. The model represents material torsion using rotation angles with respect to the Bishop frame [Bis75] of its centerline. Its simulation efficiency is achieved using dynamic simulation of centerline and quasistatic simulation of material frame. In [Had06], Hadap developed a linear time, implicit and fully recursive scheme of rigid-body chains for dynamic simulation of ears, braids, hairs, and foliage.

Cosserat theory [Ant95, Rub00] formulates a more general model of physics-based elastic rods. It was first introduced to the computer graphics community by Pai [Pai02] for interactive simulation of suture strands in laparoscopic surgery. He applied quasistatic simulation to the surgical thread based on user-specified fixed position of one end of the thread and stress at the other end. Bertails et al. used a similar approach to predict static states of hair styles [BAQ*05]. They further extended the approach to a super-helices model for dynamic simulation of hair motion [BAC*06]. A hair strand is modeled as a sequence of smooth helix segments, where each segment has constant curvature and torsion. Grégoire et al. applied quasistatic simulation of Cosserat rod to cable routing and assembly [GS07]. In modeling torsion, they used quaternions to represent the orientation of each discrete segment of the rod. Spillmann and Teschner [ST07, ST08] used a similar rod representation for interactive simulation of dynamic ropes and knots. Their method allows the user to easily manipulate any portion of the rope.

Most of the existing methods focus on simulating thin rods with small and rigid cross-sections. According to the application requirements, some of them also assume that the rod is inextensible or unshearable. These conditions are not valid for hollow tubes with large and deformable cross-sections. Therefore, existing rod simulation methods cannot be directly used for simulating hollow tubes. So far, the simulation of hollow tubes with large and deformable cross-sections has not been sufficiently studied in the literature.

To simulate hollow tubes with deformable cross-sections for studying the mechanics of carbon nanotubes, Gould and Burton [GB06] presented a model that uses a sequence of Cosserat rings to represent the tube's cross-sections. The rings are assumed to be planar, and are assembled to represent the bending, shearing and twisting of the tube. This approach is physically accurate but is very complex and com-
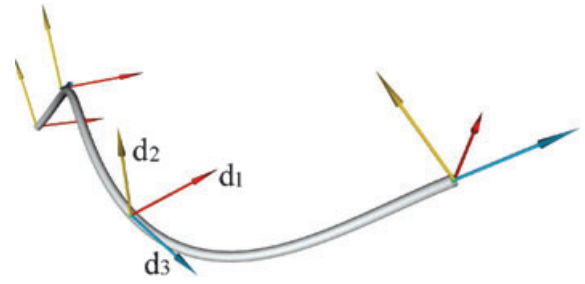
Figure 2: *A Cosserat rod. Arrows depict the directors.*

putationally expensive. In comparison, our model of hollow tube is easier to implement and computationally less expensive than that of Gould and Burton. Simulation tests show that our approach can produce realistic results for the deformation of various kinds of elastic hollow tubes.

It is interesting to note that the binding of mesh surface to the reference Cosserat rod in our hybrid model is similar in nature to the skinning of animated characters, i.e., the binding of skin to bones [AS07, JZvdP*08]. The difference is that our reference rod is a deformable curve whereas the bones in the animated characters are rigid objects connected by articulated joints.

3. Hybrid Model of Elastic Tubes

Our hybrid model of a hollow tube consists of a reference Cosserat rod (Section 3.1) and the surface of the tube. For a given surface model of a tubular object, we first construct the hybrid model by fitting a reference rod to the centerline of the surface (Section 4). A binding relationship between the surface model and the reference rod is then established. The deformation of the tube is achieved by first deforming the reference rod according to Cosserat theory and the user specified boundary conditions (Section 5.1). Then, the surface model is deformed according to the surface elastic energy and the established binding relationship to the reference rod (Section 5.2).

3.1. Cosserat rod

A Cosserat rod C [Ant95, LCW04] is described by a 3D curve $\mathbf{r}(s, t)$, directors $\mathbf{d}_k(s, t)$ with $k \in \{1, 2, 3\}$, the arc length parameter $s \in [0, L]$, and the time parameter t (Figure 2). The directors $\mathbf{d}_k(s, t)$ are orthonormal vectors following the right-handed rule, i.e., $(\mathbf{d}_1 \times \mathbf{d}_2) \cdot \mathbf{d}_3 > 0$. They are defined as follows. $\mathbf{d}_3(s, t)$ is normal to the cross-sectional plane $\mathcal{X}_s$ of the rod at s. $\mathbf{d}_1(s, t)$ is in $\mathcal{X}_s$ and points at a material point p_s on the rod's surface. $\mathbf{d}_2 = \mathbf{d}_3 \times \mathbf{d}_1$ points to another material point. $\mathbf{d}_k$ must be differentiable such that the material points represented by $\mathbf{d}_1$ and $\mathbf{d}_2$ form continuous material lines.

The reference configuration of a Cosserat rod, $C^0 = \{\mathbf{r}^0(s), \mathbf{d}_k^0(s)\}$, is the initial state of the rod at time $t = 0$:

$$\mathbf{r}^0(s) \equiv \mathbf{r}(s, 0), \qquad \mathbf{d}_k^0(s) \equiv \mathbf{d}_k(s, 0). \qquad (1)$$

Typically in mechanical engineering, C^0 is considered as a straight rod for analytical simplicity. But, it can also be a naturally curved rod [Lov27, Vil98].

The deformed configuration, $C^T = \{\mathbf{r}^T(s), \mathbf{d}_k^T(s)\}$, is the equilibrium state of the rod at time $t = T$:

$$\mathbf{r}^T(s) \equiv \mathbf{r}(s, T), \qquad \mathbf{d}_k^T(s) \equiv \mathbf{d}_k(s, T). \qquad (2)$$

For notational simplicity, we ignore the parameter t when there is no confusion.

3.2. Stress, strain and potential energy

The strains of a Cosserat rod are classified into *linear strain vector* $\boldsymbol{v}(s)$ and *angular strain vector* $\boldsymbol{u}(s)$ [Ant95] such that

$$\boldsymbol{v}(s) = \partial_s \mathbf{r}(s), \qquad \partial_s \mathbf{d}_k(s) = \boldsymbol{u}(s) \times \mathbf{d}_k(s). \qquad (3)$$

The strain vectors $\boldsymbol{u}(s)$ and $\boldsymbol{v}(s)$ can be resolved into three components by the directors $\mathbf{d}_k$:

$$\boldsymbol{u} = \sum_k u_k \mathbf{d}_k, \qquad \boldsymbol{v} = \sum_k v_k \mathbf{d}_k, \qquad (4)$$

where u_k and v_k are the *strain variables*. The components u_1 and u_2 of the curvature along $\mathbf{d}_1$ and $\mathbf{d}_2$ measure bending, while u_3 measures torsion. The components v_1 and v_2 measure shear, and v_3 measures stretching or elongation. Let us denote

$$\mathbf{u} \equiv [u_1, u_2, u_3]^\top, \qquad \mathbf{v} \equiv [v_1, v_2, v_3]^\top. \qquad (5)$$

Note that the vectors $\boldsymbol{u}$ and $\boldsymbol{v}$ should be distinguished from $\mathbf{u}$ and $\mathbf{v}$. The former is defined in the global coordinate system, whereas the latter is defined according to the directors.

Assuming the Kirchhoff constitutive relations [GB06, Lov27, Vil98], the couple (i.e., inner torque) $\mathbf{m}(s)$ and stress $\mathbf{n}(s)$ experienced by the rod are

$$\mathbf{m}(s) = \mathbf{J}(s)(\mathbf{u}(s) - \mathbf{u}^0(s)), \qquad \mathbf{n}(s) = \mathbf{K}(s)(\mathbf{v}(s) - \mathbf{v}^0(s)). \qquad (6)$$

$\mathbf{J}(s)$ and $\mathbf{K}(s)$ are stiffness matrices that depend on the geometric shape and material properties of the rod:

$$\mathbf{J}(s) = \mathrm{diag}\{Y I_1(s), Y I_2(s), G I_3(s)\}, \qquad (7)$$

$$\mathbf{K}(s) = \mathrm{diag}\{G A(s), G A(s), Y A(s)\}, \qquad (8)$$

where Y is the Young's modulus, G the shear modulus, $A(s)$ the cross-sectional area, and $I_k(s)$ the geometric moments of inertia of the cross-section at s. For a hollow tube of circular

cross-sections with inner and outer radii $R_i(s)$ and $R_o(s)$,

$$I_1(s) = I_2(s) = \pi \left(R_o^4(s) - R_i^4(s) \right) / 4,$$

$$I_3(s) = \pi \left(R_o^4(s) - R_i^4(s) \right) / 2,$$

$$A(s) = \pi \left(R_o^2(s) - R_i^2(s) \right). \qquad (9)$$

The potential energy at point s of the rod is [Ant95]:

$$\mathcal{E}(s) = \frac{1}{2}[(\mathbf{u}(s) - \mathbf{u}^0(s))^\top \mathbf{m}(s) + (\mathbf{v}(s) - \mathbf{v}^0(s))^\top \mathbf{n}(s)] \qquad (10)$$

and the total potential energy of the rod is:

$$\mathcal{E} = \int_0^L \mathcal{E}(s) \, ds. \qquad (11)$$

The final configuration $C^T = \{\mathbf{r}^T, \mathbf{d}_k^T\}$ is the equilibrium state of the rod, with minimum potential energy $\mathcal{E}$ that minimizes the difference between $\mathbf{u}^T$, $\mathbf{v}^T$ and $\mathbf{u}^0$, $\mathbf{v}^0$.

3.3. Representation of directors

A Cosserat rod is represented by the tuple $\{\mathbf{r}(s), \mathbf{d}_k(s)\}$. This representation has a total of 12 variables for each s, subject to the orthonormal constraints of the directors (6 constraints). Thus, there are only 6 independent variables, 3 for position $\mathbf{r}_s$ and 3 for orientation of $\mathbf{d}_k(s)$.

The director frame can be regarded as a rotation R with respect to a global reference frame $(\mathbf{d}_X, \mathbf{d}_Y, \mathbf{d}_Z)$ such as the world coordinate frame:

$$\mathbf{d}_1(s) = R(s)\mathbf{d}_X, \qquad \mathbf{d}_2(s) = R(s)\mathbf{d}_Y, \qquad \mathbf{d}_3(s) = R(s)\mathbf{d}_Z, \qquad (12)$$

where $\mathbf{d}_X$, $\mathbf{d}_Y$, and $\mathbf{d}_Z$ are unit vectors along the X-, Y-, Z-axes. The most straightforward way to represent the rotation R is to use rotation matrix. But it requires 6 orthonormal constraints. So, it has no advantage over the direct use of $\mathbf{d}_k$ as variables.

To reduce redundant variables and constraints, one possible method is to use Euler angles, which represent 3D rotation using only 3 variables. However, they are not natural and continuous for interpolation and differentiation, and they have the classical Gimbal lock problem.

Another popular method is to use quaternions. A quaternion represents 3D rotation using 4 variables and 1 constraint: it has unit length. Quaternion has been used in elastic rod simulation (e.g., [GS07, ST07]). However, it has limitations too. First, a quaternion and its negative vector represent the same rotation, which may cause ambiguity when computing the strain variables. Second, it still comes with one constraint, which has to be either explicitly or implicitly enforced in the energy term.

In our model, we adopt Rodrigues' rotation formula to represent the directors. This formula represents 3D rotation

by a rotation axis $\hat{\mathbf{n}}$ and a rotation angle θ. The rotation $R(s)$ can be expressed by a vector $\mathbf{q}(s) = [q_1(s), q_2(s), q_3(s)]^\top$ such that:

$$\mathbf{q}(s) = \theta(s)\hat{\mathbf{n}}(s). \tag{13}$$

In contrast to the other representations, this method is constraint-free, continuous for interpolation and differentiation, and does not have ambiguity problem.

At first sight, it seems that this rotation vector $\mathbf{q}$ has a similar ambiguity problem as quaternions, i.e., $(\theta + 2k\pi)\hat{\mathbf{n}}$, with k an arbitrary integer, represent the same director. However, it turns out that this property is beneficial to our model. If the rod is discretized to a sequence of points, there can be situations in which the directors of two consecutive points are the same, but in between the two points, the rod actually experiences a rotation of 2π. The discrete directors cannot capture the rotation in the middle. They will only generate zero torsion because the changes of directors of the two consecutive points are zero. However, our rotation vector can capture the correct strain values in this situation: the two consecutive points have rotation $\theta\hat{\mathbf{n}}$ and $(\theta + 2\pi)\hat{\mathbf{n}}$ respectively. In this case, the resulting directors are the same, but the torsion values are non-zero.

With the rotation vector $\mathbf{q}$ and the global reference frame $(\mathbf{d}_X, \mathbf{d}_Y, \mathbf{d}_Z)$, the directors can then be expressed as:

$$\mathbf{d}_1 = \frac{1}{\|\mathbf{q}\|^2} \left[1 - b\left(q_2^2 + q_3^2\right), bq_1q_2 + aq_3, bq_1q_3 - aq_2 \right]^\top,$$

$$\mathbf{d}_2 = \frac{1}{\|\mathbf{q}\|^2} \left[bq_1q_2 - aq_3, 1 - b\left(q_1^2 + q_3^2\right), bq_2q_3 + aq_1 \right]^\top,$$

$$\mathbf{d}_3 = \frac{1}{\|\mathbf{q}\|^2} \left[bq_1q_3 + aq_2, bq_2q_3 - aq_1, 1 - b\left(q_1^2 + q_2^2\right) \right]^\top, \tag{14}$$

where $a = \sin\|\mathbf{q}\|/\|\mathbf{q}\|$, and $b = (1 - \cos\|\mathbf{q}\|)/\|\mathbf{q}\|^2$. Now we have 6 variables $\{\mathbf{r}(s), \mathbf{q}(s)\}$ for each s.

The strain variables u_k and v_k and the potential energy E can also be expressed in terms of $\{\mathbf{r}(s), \mathbf{q}(s)\}$. The variables v_k are relatively easy to compute from (4):

$$v_k = \mathbf{d}_k \cdot \mathbf{v} = \mathbf{d}_k \cdot \partial_s \mathbf{r}. \tag{15}$$

The derivation of variables u_k is mathematically more involved. It is similar to the one presented in [ST07], except that Rodrigues' formula is used instead of quaternions to represent rotation. For completeness, we derive the expressions of $\mathbf{u}_k$ in Appendix A and refer to [ST07] for details.

3.4. Binding surface model to cosserat rod

The continuous surface of a tube can be considered as a shape function defined by the rod. For each point $\mathbf{p}$ on the surface, there exists an s such that $\mathbf{p}$ is on the cross-section $\mathcal{X}_s$ of the tube at s. A one-to-one binding function $\mathbf{f}$ can then

be established between the local coordinates (x, y, z) in the directors $\mathbf{d}_k$ at s and the global coordinates $\mathbf{p}$:

$$\begin{aligned} \mathbf{p} &= \mathbf{f}(s, x, y, z) \\ &= \mathbf{r}(s) + x\,\mathbf{d}_1(s) + y\,\mathbf{d}_2(s) + z\,\mathbf{d}_3(s). \end{aligned} \tag{16}$$

We say that mesh vertex $\mathbf{p}$ is mapped to $\mathbf{r}(s)$ and $\mathbf{d}_k(s)$ of the reference rod. Since $\mathbf{p}$ is on the cross-section $\mathcal{X}_s$ and $\mathbf{d}_3$ is the normal of $\mathcal{X}_s$, z is usually 0 in continuous case, and close to zero in discrete case. Given any configuration of the rod and the binding function $\mathbf{f}$, the tube's surface can be reconstructed.

When an elastic tube deforms, its surface stretches and bends. The continuous formulation of surface deformation is thus founded on the measure of stretching and bending energies. Stretching and bending can be measured by the changes of first and second fundamental forms [BS08] respectively. For discrete mesh models, various techniques have been presented to correctly estimate the energies (e.g., [GB06]). Since stretching and bending are essentially non-linear characteristics, the resulting deformable model are usually non-linear, which can be computationally expensive. For efficient and realistic deformation of surface mesh models, a popular approach is Laplacian deformation [BS08, MYF06, MDSB02, SLCO*04], which approximates the surface elastic energy use linear Laplacian operators. Details of the method are discussed in Section 5.2.

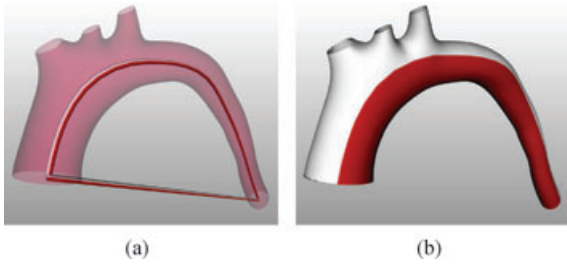### 4. Construction of Hybrid Model

Our method requires only the surface mesh model of an elastic tube as the input. Given the mesh, a hybrid model is constructed. The construction of the hybrid model proceeds in two stages, given the initial configuration of the mesh. First, a generalized cylinder defined by the centerline and cross-sectional radii of the tube is computed (Section 4.1). The reference rod for C^0 is defined to coincide with the centerline, and its geometric moments of inertia are approximated using the cross-sectional radii and (9). Then, rotation minimizing frames (RMFs) [Klo86, WJZL08] are used to generate the directors in C^0 (Section 4.2), which yield the initial strain variables $\mathbf{u}^0$ and $\mathbf{v}^0$. For simplicity, we assume that the initial configuration C^0 of the tube is not sheared and is minimally twisted.

4.1. Fitting generalized cylinder

Let $\mathbf{p}_i$ denote a surface point that is in the cross-section $\mathcal{X}_s$ at point s on the centerline. Then, the coordinate $\mathbf{r}(s)$ of the point s on the centerline would be the centroid of such $\mathbf{p}_i$'s:

$$\mathbf{r}(s) = \frac{1}{N_s} \sum_{\mathbf{p}_i \in \mathcal{X}_s} \mathbf{p}_i \tag{17}$$

where N_s is the number of points in $\mathcal{X}_s$. In the case of a discrete 3D mesh model, the points $\mathbf{p}_i$ are taken as the mesh vertices. Then, the centerline cannot be defined using (17)

(a)   (b)

Figure 3: *Hybrid model construction. (a) Fitting the centerline of the mesh model. The fitting algorithm starts from a straight line connecting the centers of the tube's two ends, and computes the curve that matches the centerline. (b) Texture mapping the mesh surface according to the binding facilitates visualization of bending and torsion.*

because for each s, the number of mesh vertices that exactly lie on the cross-section $\mathcal{X}_s$ may be limited and unbalanced. Instead, the centerline is defined in terms of the mesh vertices $\mathbf{p}_i$ whose normal projections on the centerline are close to $\mathbf{r}(s)$:

$$\mathbf{r}(s) = \sum_i w_i(s)\mathbf{p}_i \left[\sum_i w_i(s) \right]^{-1}. \qquad (18)$$

The weights $w_i(s)$ are inversely related to the distance between $\mathbf{r}(s)$ and the projection of $\mathbf{p}_i$. In the implementation, the weights are defined in terms of a Gaussian function. Note that this definition of centerline is implicit because the corresponding s of a mesh vertex $\mathbf{p}_i$ is not known in advance. Thus, a fitting algorithm is needed to find the centerline of the mesh model.

The fitting algorithm defines a cost function to evaluate the goodness of fit and applies gradient decent to optimize the cost function [KWL06] starting from a straight line connecting the centers of the tube's two ends (Figure 3). The cost $E(\mathbf{r})$ of fitting is derived from (18):

$$E(\mathbf{r}) = \frac{1}{2} \int_0^L \left\| \mathbf{r}(s) - \frac{\sum_i w_i(s)\mathbf{p}_i}{\sum_i w_i(s)} \right\|^2 ds + \frac{\lambda}{2} \int_0^L \|\mathbf{r}'(s)\|^2 ds, \qquad (19)$$

where $\mathbf{r}'(s)$ is the first derivative of $\mathbf{r}(s)$. The second term is a regularization term that enforces smoothness of the fitted curve and λ is the regularization parameter.

Applying variational calculus to (19) yields the following iterative update formula for $\mathbf{r}(s)$:

$$\Delta\mathbf{r} = \eta \left[-\sum_i w_i(s)[\mathbf{r}(s) - \mathbf{p}_i] \left[\sum_i w_i(s) \right]^{-1} + \lambda\,\mathbf{r}''(s) \right] \qquad (20)$$

where $\mathbf{r}''(s)$ is the second derivative of $\mathbf{r}(s)$, and η is a constant step size.

After fitting the centerline, the radius at each cross-section is computed so as to derive the stiffness matrices $\mathbf{J}$ and $\mathbf{K}$ in (7) and (8). The cost function $E(R)$ for fitting the radius function $R(s)$ is given by:

$$E(R) = \frac{1}{2} \int_0^L \left[R(s) - \frac{\sum_i \|\mathbf{r}(s) - \mathbf{p}_i\|}{N_s} \right]^2 ds$$
$$+ \frac{\mu}{2} \int_0^L R'(s)^2\, ds, \qquad (21)$$

where the first term approximates the radius and the second term regularize the radius function $R(s)$ with μ the regularization parameter.

Applying variational calculus to (21) yields

$$\Delta R = \eta \left[-R(s) + \frac{1}{N_s} \sum_i \|\mathbf{r}(s) - \mathbf{p}_i\| + \mu R''(s) \right]. \qquad (22)$$

4.2. Deriving directors and binding function

The initial configuration C^0 is the rest state of the tubular object. We assume there is no shearing, twisting, and elongation at the rest state, i.e., $\mathbf{d}_3$ aligns with the tangent of the centerline. Note that the object may be naturally curved (e.g, blood vessel and hair), so the directors should be defined to represent the natural bending and torsion, but nothing extra.

One way to define the directors for the natural state of a curve is to use the Frenet frame, whose three axis vectors are the tangent, principle normal and bi-normal of the centerline at s. However, Frenet scheme is ill-defined at an inflection point, where the curvature and normal change sign. This results in the undesirable flipping of the directions of the Frenet frames.

Another way to define the initial directors is to use RMF [Bis75, Klo86, WJZL08]. A RMF is a moving frame along the centerline that minimizes the amount of rotation of the frame. RMF has desirable properties for describing torsion and bending in the initial state. So, we use RMF to define the initial directors in C^0.

It is very difficult to compute the exact RMF for a general spline curve [WJZL08]. A projection method [Klo86] and a rotation method [Blo90] can be used to approximate discrete RMF. These methods have second-order global approximation error [CW96]. Wang et al. [WJZL08] presented a simple and efficient algorithm to approximate RMF, namely double reflection method. Their method has fourth-order global approximation error, and is thus more accurate than the first two. In this paper, we adopt the double reflection method to generate the directors in the initial configuration.

The mapping function $\mathbf{f}$ that binds the mesh vertices to the rod is determined according to (16):

$$\mathbf{p}_i = \mathbf{r}(s) + x_i\mathbf{d}_1(s) + y_i\mathbf{d}_2(s) + z_i\mathbf{d}_3(s). \qquad (23)$$

where s is $\mathbf{p}_i$'s corresponding parameter on the reference rod.

5. Discrete Implementation of Elastic Tubes

An elastic hollow tube behaves globally like a rod even if its deformation undergoes cross-sectional changes. So, global deformation and cross-sectional deformation can be decoupled into two phases. First, the reference rod is deformed according to Cosserat theory and user-specified boundary conditions (Section 5.1). Next, the mesh is deformed using Laplacian deformation according to its elastic binding to the rod and its surface elastic energy (Section 5.2).

5.1. Discretization of cosserat potential energy

Let us discretize the reference rod parameterized by $s \in [0, L]$ into $N - 1$ segments, and $\mathbf{r}_i$ denote the starting point of segment i, $i = 1, 2, \ldots, N - 1$, and $i = N$ denote the end point of segment $N - 1$. The model's configuration is now given by $(\mathbf{r}_i, \mathbf{q}_i)$. The first derivatives of $\mathbf{q}_i$ and $\mathbf{r}_i$ are estimated by backward finite difference:

$$\partial_s \mathbf{q}_i = \frac{\mathbf{q}_i - \mathbf{q}_{i-1}}{l_i}, \qquad \partial_s \mathbf{r}_i = \frac{\mathbf{r}_i - \mathbf{r}_{i-1}}{l_i}, \qquad (24)$$

with $\partial_s \mathbf{q}_1 \equiv \partial_s \mathbf{q}_2$ and $\partial_s \mathbf{r}_1 \equiv \partial_s \mathbf{r}_2$. The discrete potential energy can be written as:

$$\mathcal{E} = \sum_{i=1}^{N-1} \frac{l_i}{2} (\mathcal{E}_i + \mathcal{E}_{i+1}) = \sum_{i=1}^{N} \bar{l}_i \mathcal{E}_i \qquad (25)$$

where l_i is the segment length at rest state, $\bar{l}_i = (l_{i-1} + l_i)/2$ (we define $l_0 = l_N = 0$ to make $\bar{l}_i$ valid for every i), and

$$\mathcal{E}_i = \frac{1}{2} \left[\left(\mathbf{u}_i - \mathbf{u}_i^0 \right)^\top \mathbf{K}_i \left(\mathbf{u}_i - \mathbf{u}_i^0 \right) + \left(\mathbf{v}_i - \mathbf{v}_i^0 \right)^\top \mathbf{J}_i \left(\mathbf{v}_i - \mathbf{v}_i^0 \right) \right] \qquad (26)$$

To manipulate the reference rod, we can specify boundary conditions on the rod. There are three types of boundary conditions for manipulating the rod:

Type 1. Specify the position $\mathbf{r}_i$.
Type 2. Specify the orientation $\mathbf{q}_i$.
Type 3. Specify the orientation of one of the three directors.

Under the specified boundary conditions, quasi-Newton algorithm [PTVF02] is applied to minimize the total potential energy, which yields the deformed configuration of the rod that satisfies the boundary conditions.

5.2. Laplacian surface deformation

Laplacian method [BS08, MYF06, MDSB02, SLCO*04] deforms a mesh model by minimizing the change of mean curvature normals of the surface points. Other geometric conditions can be easily added to constrain the deformation. In our model, surface bending (Section 5.2.1), surface stretching (Section 5.2.2), and surface binding (Section 5.2.3) are formulated to constrain the Laplacian deformation.

5.2.1. *Surface bending*

Surface bending can be measured by the change of curvature at each point $\mathbf{p}$ on the surface. Curvature is estimated by the Laplacian operator $\mathbf{l}(\mathbf{p})$:

$$\mathbf{l}(\mathbf{p}) = \sum_{\mathbf{p}_i \in N(\mathbf{p})} w_i (\mathbf{p} - \mathbf{p}_i) \qquad (27)$$

where $N(\mathbf{p})$ is the set of neighboring points connected to $\mathbf{p}$ in the mesh. The magnitude of $\mathbf{l}(\mathbf{p})$ approximates the mean curvature at $\mathbf{p}$, and the direction of $\mathbf{l}(\mathbf{p})$ approximates its normal. The weight w_i can be either uniform weight or cotangent weight [MDSB02]. In our case, we adopt the former for simplicity, i.e., $w_i = 1/|N(\mathbf{p})|$, where $|N(\mathbf{p})|$ is the number of neighboring points connected to $\mathbf{p}$.

Surface bending energy is defined as the change of Laplacian before and after deformation:

$$E_b(\mathbf{p}) = k_b \|\mathbf{l}(\mathbf{p}) - \mathbf{l}^0(\mathbf{p})\|_2^2, \qquad (28)$$

where $\mathbf{l}^0(\mathbf{p})$ is the Laplacian of $\mathbf{p}$ at the initial configuration of the surface and k_b is the bending stiffness.

The formulation of (28) suffers from the shortcoming that $\mathbf{l}^0(\mathbf{p})$ is defined in the world coordinate system. By minimizing $E_b(\mathbf{p})$, the Laplacian method requires the new $\mathbf{l}(\mathbf{p})$ to be close to $\mathbf{l}^0(\mathbf{p})$, which creates undesirable distortion of the object's shape when the object deformation causes a change of orientation of a local patch (Figure 4). To handle this problem, rotation-invariant Laplacian methods have been proposed [BS08, MYF06]. For example, the method of Masuda et al. computes rotation-invariant Laplacians by approximating the rotations of the normals at the mesh vertices. In our model, rotation-invariance is achieved by measuring the Laplacians with respect to the directors of the reference rod, which are intrinsic properties of the rod. This is a more natural approach to achieving rotation invariance of Laplacian for tubular objects.

For each point $\mathbf{p}$, the rotation of its local patch can be considered as the rotation of $\mathbf{p}$'s associated directors, which can be directly approximated from the reference rod. Let us denote as $\mathbf{R}(\mathbf{p})$ the rotation of $\mathbf{p}$'s associated directors. The bending energy can then be expressed as:

$$E_b(\mathbf{p}) = k_b \|\mathbf{l}(\mathbf{p}) - \mathbf{R}(\mathbf{p}) \mathbf{l}^0(\mathbf{p})\|_2^2, \qquad (29)$$
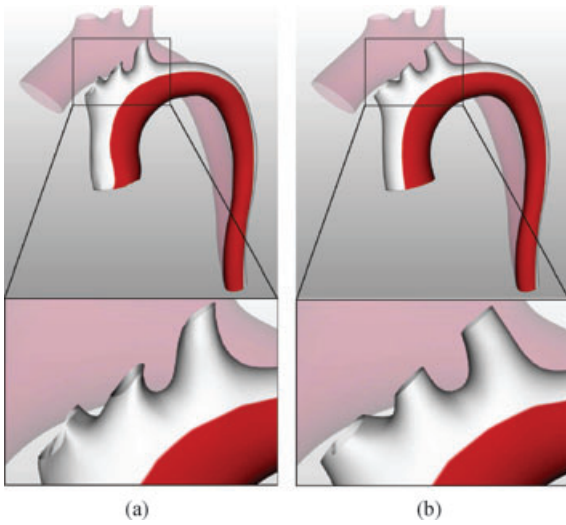
Figure 4: *Rotation-invariant Laplacian deformation. (a) Non-rotation-invariant Laplacian deformation distorts surface details. (b) Rotation-invariant Laplacian deformation produces no distortion. The lighter model denotes the initial configuration, and the brighter model denotes the deformed configuration.*

In this way, the rotated Laplacian operator is invariant to rotation of local patches (Figure 4). This method of computing rotation-invariant Laplacian is accurate as long as the rotation of the local patch is close to the rotation of the associated directors, regardless of the complexity of the surface geometry. Empirical test shows that this condition is met in our application domain. Nevertheless, for more general cases where the rotation of local patches differs a lot from that of the rod segments, further investigation is necessary for a more precise evaluation of the local rotation.

Assembling (29) for each point gives the total bending energy E_b:

$$E_b = \|\mathbf{L}\mathbf{x} - \mathbf{u}\|_2^2. \tag{30}$$

The term $\mathbf{L}\mathbf{x}$ contains $\mathbf{l}(\mathbf{p})$, $\mathbf{u}$ contains $\mathbf{R}(\mathbf{p})\mathbf{l}^0(\mathbf{p})$, and $\mathbf{x}$ is the vector of coordinates of all the mesh points.

5.2.2. Surface stretching

Surface stretching energy is measured by the change of edge lengths similar to [Gri06]. For every edge $\mathbf{e}$ that connects points $\mathbf{p}_i$ and $\mathbf{p}_j$ in the mesh, the stretching energy is formulated as

$$E_s(\mathbf{e}) = k_s \left(\left\|\mathbf{p}_i - \mathbf{p}_j\right\| - \left\|\mathbf{p}_i^0 - \mathbf{p}_j^0\right\| \right)^2, \tag{31}$$

where k_s is the stretching stiffness and is related to the Young's modulus Y by the formula $k_s = Y/(2\|\mathbf{p}_i^0 - \mathbf{p}_j^0\|)$.

This energy term is non-linear because of the Euclidean distances. In order to facilitate the optimization (Section 5.2.4), we write it in its equivalent form:

$$E_s(\mathbf{e}) = k_s \|\mathbf{d}_{ij} - \mathbf{s}_{ij}\|_2^2 \tag{32}$$

where

$$\mathbf{d}_{ij} = \mathbf{p}_i - \mathbf{p}_j, \qquad \mathbf{s}_{ij} = \mathbf{d}_{ij} \frac{\left\|\mathbf{p}_i^0 - \mathbf{p}_j^0\right\|}{\|\mathbf{p}_i - \mathbf{p}_j\|}. \tag{33}$$

Assembling the edge stretching energy together gives the total stretching energy E_s to be minimized:

$$E_s = \|\mathbf{D}\mathbf{x} - \mathbf{s}(\mathbf{x})\|_2^2 \tag{34}$$

where $\mathbf{D}\mathbf{x}$ contains $\mathbf{d}_{ij}$ terms and $\mathbf{s}(\mathbf{x})$ contains $\mathbf{s}_{ij}$ terms. Note that in this case $\mathbf{D}$ is a fixed matrix.

5.2.3. Surface binding

The deformed reference rod obtained in the first phase of the algorithm defines a corresponding mesh surface according to the binding function (23). This mesh surface cannot be used directly as the deformed surface of the elastic tube because it does not account for elastic surface deformation. Nevertheless, the vertices of the mesh can be used as soft constraints for applying Laplacian deformation on the initial mesh to generate realistic deformed surface. We denote the vertices of this corresponding mesh as $\mathbf{p}^1$. The surface binding energy is thus:

$$E_x(\mathbf{p}) = k_x \|\mathbf{p} - \mathbf{p}^1\|_2^2 \tag{35}$$

where k_x is the corresponding binding coefficient. Assembling (35) for all the points generates:

$$E_x = k_x \|\mathbf{F}\mathbf{x} - \mathbf{w}\|_2^2 \tag{36}$$

where $\mathbf{F}\mathbf{x}$ contains $\mathbf{p}$ terms and $\mathbf{w}$ contains $\mathbf{p}^1$ terms. The value of binding coefficient k_x determines the amount of cross-sectional change allowed. If k_x is very large, the cross-sections of the tube will not change too much, and the overall behaviour of the tube will be like a Cosserat rod. The effect of the binding coefficient will be discussed in Section 6.

5.2.4. Surface deformation

The total energy E to be minimized is:

$$E = E_b + E_s + E_x \tag{37}$$

which is equivalent to minimizing

$$\|\mathbf{K}\mathbf{x} - \mathbf{z}(\mathbf{x})\|_2^2 \tag{38}$$

where $\mathbf{K} = (\mathbf{L}^\top \mathbf{D}^\top \mathbf{F}^\top)^\top$ and $\mathbf{z}(\mathbf{x}) = (\mathbf{u}^\top (\mathbf{s}(\mathbf{x}))^\top \mathbf{w}^\top)^\top$.

This is a non-linear optimization problem. However, the matrix $\mathbf{K}$ is a fixed sparse matrix during the whole simulation process. So, its pseudo-inverse can be precomputed

before simulation. During the optimization process, backward substitution is applied to solve the system as demonstrated in [WXW*06]. In this way, surface deformation can be efficiently solved even though (37) contains non-linear stretching energy.

5.3. Quasistatic simulation

There are two current approaches for simulating deformation of elastic objects: dynamic simulation and quasistatic simulation [TGDM07]. Dynamic simulation models object motion based on Newtonian or Lagrangian equation of motion. It generates dynamic transition between the object's rest states. On the other hand, quasistatic simulation assumes that the system goes through a sequence of states that are infinitesimally close to equilibrium. Given the boundary conditions specified by the user, quasistatic simulation minimizes the object's energy function to generate a sequence of equilibrium states.

Dynamic simulation can generate physically accurate motion if the time step and time integration scheme are properly chosen. However, it is computationally more expensive than quasistatic simulation for generating static solutions [TGDM07]. Quasistatic simulation provides accurate simulation results at equilibrium states, but does not guarantee smoothness and correctness in state transition. For example, it does not simulate oscillation. In interactive design and modeling of complex objects, where the response speed and accurate final states are more important than state transitions, quasistatic simulation is preferred. In our simulation, since our target problems are static problems, we apply quasistatic simulation for its simplicity and efficiency.

Our quasistatic simulation algorithm works as follows. Given the user specified boundary conditions that defines the deformation of the tube, the algorithm first interpolates the boundary conditions for the intermediate simulation steps. Then, for each simulation step, the static solution of the reference Cosserat rod is computed using quasi-Newton optimization algorithm in [PTVF02]. After that, the surface deformation energy is optimized to generate the deformed tube at the current simulation step.

6. Experimental Results and Discussions

Experiments were performed to evaluate the performance of our proposed hybrid model. Figure 1 illustrates the manipulation of an aorta model, which is naturally curved. The lower end of the aorta model (descending aorta) was fixed in both position and orientation. The upper end (ascending aorta) was moved to a lower position. In this case, there were Type 1 boundary conditions (Section 5.1) at both ends, and Type 2 boundary condition at the lower end of aorta. Our algorithm produced the configuration with minimum amount of torsion that satisfied the boundary condition at
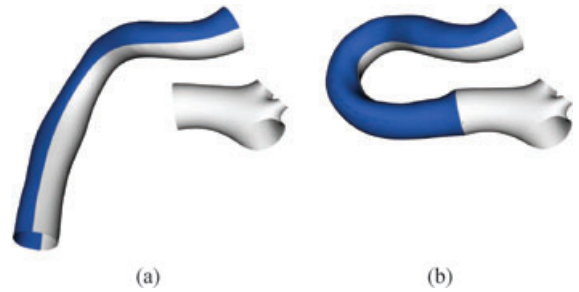
Figure 5: *Deformation and joining of vena cava model. (a) Initial configuration. (b) Vena cava is deformed and joined to another fixed blood vessel with minimum twisting.*
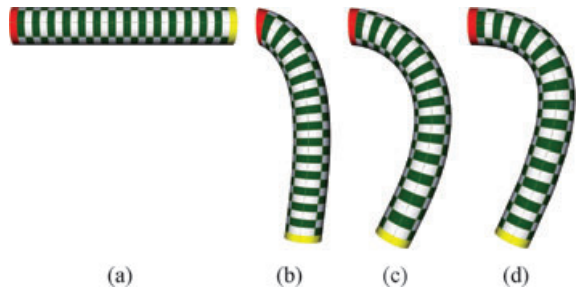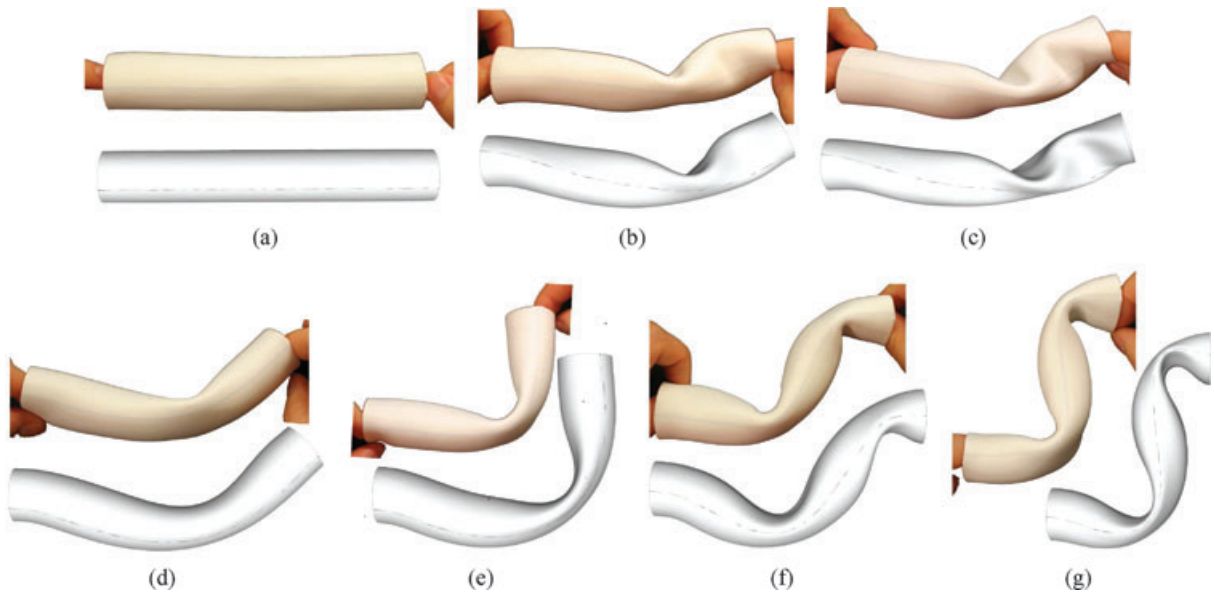

Figure 6: *Shearing of elastic tubes. (a) Initial configuration. The left end (red) is fixed in both position and orientation. The right end (yellow) is moved. (b–d) Deformation results of elastic tube with different material properties. (b) Y = 0.1, G = 0.1. (c) Y = 0.1, G = 10. (d) Y = 0.1, G = 120.*

the two ends (Figure 1(b)). For comparison, another configuration was produced by intentionally rotating the upper end about its director $\mathbf{d}_3$, which caused twisting of the aorta (Figure 1(c)). This illustrates the difference from a minimum torsion configuration.

In Figure 5, the curved vena cava model was deformed to join with another fixed blood vessel model. As the two joining shapes of the boundaries were different, the cross-sections of the vena cava model changed after joining. The joining was achieved by imposing positional and orientation constraints onto the joining boundary of the vena cava. The shape of the fixed blood vessel was regarded as unchanged.

Figure 6 evaluates shearing of elastic tubes with different material properties. In this test, the left end of the tube was fixed in both position and orientation. The right end was moved. All the three rods had the same value for Young's modulus, while their shear moduli were different. For the rod with low shear modulus (Figure 6(b)), bending and stretching were resisted, while shearing was allowed. For the rod with higher shear modulus (Figure 6(c)), the resistance to

Figure 7: *Deformation of elastic tube, compared with a real tube (upper parts of the pictures). (a) Initial configuration. (b, c) Slight bending and different amount of twisting. (d–g) Different types of bending.*
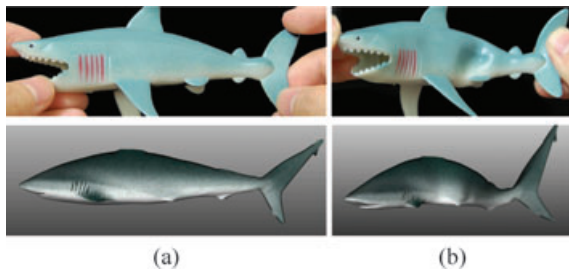
Figure 8: *Deformation of a hollow shark toy modeled by our hybrid model. (a) Initial configuration. (b) Deformed configuration.*

shearing increased. For the rod with very high shear modulus (Figure 6(d)), it was hard to shear. So, it had to bend and stretch.

Figure 7 compares our model with a real elastic tube. Both the real tube and our tube model were manipulated on their two ends. They were bent and twisted in various ways. The similarity of our tube model to the real one shows that our method can produce physically correct behaviors of the tube in various conditions, even if it undergoes large amount of cross-sectional changes.

Figure 8 illustrates that our hybrid model can also be used to model hollow objects with non-circular cross-sections. In this case, the reference rod is a straight rod connecting the head and the tail of the shark in the initial configuration. Note that the surface mesh was not acquired from scanning

the shark toy shown in the upper row. Thus, their geometric structures were different such that the deformed shapes did not look the same. However, our simulation results still correctly produced the folding effects on the model surface when it is bent. For objects that are too far from a tube-like object, the hybrid model becomes infeasible as the reference rod is not physically meaningful.

In addition to simulating the deformation of hollow elastic tube, our model can also be used to produce the effect of pressurized tubes. This is achieved through tuning the binding stiffness k_x in (35). Small k_x means the deformation depends more on the surface elastic energy, in which case the cross sections are more "hollow", corresponding to slight or no pressure. Large k_x means the deformation depends more on the reference rod, in which case the cross sections are more "solid", analogous to water running through the tube and producing high pressure. We evaluated this effect in comparison with a real water hose. Various amount of water was running through the water hose (Figure 9). In the simulation, we started with a straight tube and bent it to approximate the hand-held water hose. The test results show the contribution of the surface binding energy to the final deformation. It also shows that even though our method does not explicitly model pressure, it can produce physically plausible results that correspond to deformation due to water pressure in the hose. The simulation results are similar to the real water hose both in the shape of the tube, and in the surface details. The potential benefit of this effect is the possibility of simulating blood vessels with and without blood passing through them. Nevertheless, for more accurate simulation, pressure should be modeled explicitly.
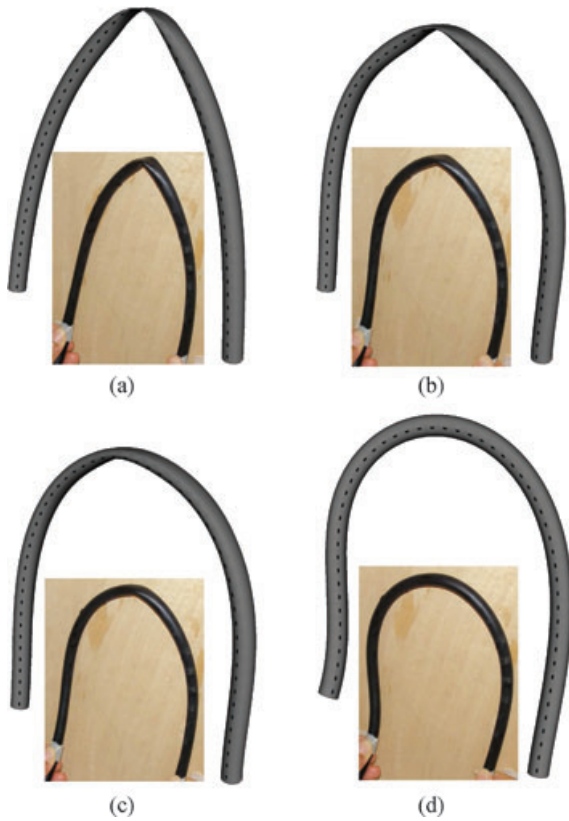
Figure 9: *Simulation of pressurized tubes. Tuning the binding stiffness k_x simulates the effects of pressurized tube. (a) $k_x = 0.01$, (b) $k_x = 0.2$, (c) $k_x = 0.5$, (d) $k_x = 2$. Dashed lines indicates material lines on the tubes' surfaces. For all the four cases, the reference rods are the same, which indicates that the reference rod does not necessarily lie inside the mesh. The smaller pictures show the real water hose.*

Table 1: *Average execution time for one simulation step.*

Fig.	# Rod elems.	# Mesh verts.	Rod def. (s)	Surface def. (s)
1	40	14148	0.58	1.42
5	30	17944	0.30	1.94
7	30	4588	0.32	0.51
8	20	7351	0.21	0.89
9	56	2368	1.01	0.24

All the experiments were carried out on a 2.33 GHz Core 2 Duo PC. The execution time for one step in the quasistatic simulation is summarized in Table 1. Normally 10 steps were performed to generate a deformed configuration. For larger amount of deformation, the number of steps were larger. For example, 20 steps were used for the deformation shown in Figure 9. Note that for applications that require only the final

deformed shape (e.g., surgical planning), Laplacian surface deformation does not have to be computed for each simulation step because it can be directly solved from the initial configuration of the surface. This can save a lot of computational time especially when the mesh model contains a large number of vertices.

7. Conclusion and Future Work

This paper presented a hybrid model for simulating the elastic deformation of hollow tubes with large, non-rigid cross-sections. For achieving accurate and efficient deformation of the elastic tube, our model binds a mesh elastically to a reference Cosserat rod. The mesh represents the surface of the hollow tube while the reference rod models bending, twisting, shearing and stretching of the tube. The deformation of the elastic tubes is accomplished in two phases. First, the reference rod is deformed according to Cosserat theory. Next, the mesh is deformed using Laplacian deformation according to the reference rod and its surface elastic energy. This hybrid approach allows the hollow tube to deform in a physically correct manner in relation to the bending, twisting, shearing, and stretching of the reference rod. It also allows the surface to deform realistically and efficiently according to surface elastic energy and the shape of the reference rod. Test results show that our model is effective in simulating the elastic deformation of hollow tubes with various shapes and material properties. In addition, it can also be used to produce realistic deformation results of pressurized tubes.

In the current implementation, quasistatic simulation is adopted because it is suitable for our target application of predictive surgical simulation. However, it should be noted that quasistatic simulation can naturally lead to discontinuities in the movement as shown in the video demo (http://www.comp.nus.edu.sg/~leowwk/heart-surgery/). For general applications such as animation, our current method needs to be extended to perform dynamic simulation. In that case, the internal force functionals can be obtained by differentiating the energy functionals (26) and (37), while the handling of contact and external forces requires further investigation because there is a need for some bilateral feedback between the rod and the surface in order to handle contact properly.

Self-collision of mesh surfaces can occur when the tubular object bends or twists sharply. In our target application of predictive surgical simulation, sharp bending and twisting of blood vessels should be avoided. Therefore, self-collision does not occur, and collision detection and handling is omitted in the current implementation. In the future, detection and handling of collisions between two or more blood vessels would be required. This may be achieved by first handling the collision of their reference rods using the method in [ST08], followed by handling the collision of their mesh surfaces using the methods in [TKZ*05].

References

[Ant95] ANTMAN S. S.: *Nonlinear Problems of Elasticity*. Springer-Verlag, 1995.

[AS07] ANGELIDIS A., SINGH K.: Kinodynamic skinning using volume-preserving deformations. In *Proc. ACM SIGGRAPH/Eurographics Symposium on Computer Animation* (2007), pp. 129–140.

[BAC*06] BERTAILS F., AUDOLY B., CANI M.-P., QUERLEUX B., LEROY F., LÉVÊQUE J.-L.: Super-helices for predicting the dynamics of natural hair. In *Proc. SIGGRAPH'06* (2006), pp. 1180–1187.

[BAQ*05] BERTAILS F., AUDOLY B., QUERLEUX B., LEROY F., LÉVÊQUE J.-L., CANI M.-P.: Predicting natural hair shapes by solving the statics of flexible rods. In *Proc. Eurographics'05 (short papers)* (2005).

[Bis75] BISHOP R. L.: There is more than one way to frame a curve. *American Mathematics Monthly 82*, 3 (1975), 245–251.

[Blo90] BLOOMENTHAL J.: Calculation of reference frames along a space curve. In *Graphics Gems* (1990), Academic Press, pp. 567–571.

[BS08] BOTSCH M., SORKINE O.: On linear variational surface deformation methods. *IEEE Transactions on Visualization and Computer Graphics 14*, 1 (2008), 213–230.

[BWR*08] BERGOU M., WARDETZKY M., ROBINSON S., AUDOLY B., GRINSPUN E.: Discrete elastic rods. In *Proc. SIGGRAPH'08* (2008), pp. 1–12.

[CDL*05] COTIN S., DURIEZ C., LENOIR J., NEUMANN P., DAWSON S.: New approaches to catheter navigation for interventional radiology simulation. In *Proc. MICCAI'05* (2005).

[CW96] CHUNG K., WANG W.: Discrete moving frames for sweep surface modeling. In *Proc. Pacific Graphics* (1996), pp. 159–173.

[GB06] GOULD T., BURTON D. A.: A Cosserat rod model with microstructure. *New Journal of Physics 8* (2006).

[GPL05] GOYAL S., PERKINS N. C., LEE C. L.: Nonlinear dynamics and loop formation in kirchhoff rods with implications to the mechanics of DNA and cables. *J. Comput. Phys. 209*, 1 (2005), 371–389.

[Gri06] GRINSPUN E.: A discrete model of thin shells. In *SIGGRAPH Courses* (2006), pp. 14–19.

[GS07] GRÉGOIRE M., SCHÖMER E.: Interactive simulation of one-dimensional flexible parts. *Computer-Aided Design 39*, 8 (2007), 694–707.

[Had06] HADAP S.: Oriented strands: dynamics of stiff multi-body system. In *Proc. ACM SIGGRAPH/Eurographics Symposium on Computer Animation* (2006), pp. 91–100.

[HMM03] HOFFMAN K. A., MANNING R. S., MADDOCKS J. H.: Link, twist, energy, and the stability of DNA minicircles. *Biopolymers 70*, 2 (2003), 145–157.

[JZvdP*08] JU T., ZHOU Q.-Y., VAN DE PANNE M., COHEN-OR D., NEUMANN U.: Reusable skinning templates using cage-based deformations. *ACM Trans. Graph. 27*, 5 (2008), 1–10.

[Klo86] KLOK F.: Two moving coordinate frames for sweeping along a 3D trajectory. *Comput. Aided Geom. Des. 3*, 3 (1986), 217–229.

[KWL06] KIRCHBERG K. J., WIMMER A., LORENZ C. H.: Modeling the human aorta for MR-driven real-time virtual endoscopy. In *Proc. MICCAI* (2006), pp. 470–477.

[LCDN06] LENOIR J., COTIN S., DURIEZA C., NEUMANN P.: Interactive physically-based simulation of catheter and guidewire. *Computers & Graphics 30*, 3 (2006), 416–422.

[LCW04] LIU D., CAO D. Q., WANG C. H.-T.: Computational Cosserat dynamics in MEMS component modelling. In *Proc. World Congress on Computational Mechanics* (2004).

[LLHH09] LI H., LEOW W. K., HUANG C.-H., HOWE T. S.: Modeling and measurement of 3D deformation of scoliotic spine using 2D x-ray images. In *Proc. Computer Analysis of Images and Patterns* (2009).

[LLQC09] LI H., LEOW W. K., QI Y., CHIU I.-S.: Predictive surgical simulation of aorta reconstruction in cardiac surgery. *Studies in Health Technology and Informatics 142* (2009), 159–161.

[Lov27] LOVE A.: *A Treatise on the Mathematical Theory of Elasticity*, 4th ed. Cambridge University Press, 1927.

[LPY04] LACARBONARA W., PAOLONE A., YABUNO H.: Modeling of planar nonshallow prestressed beams towards asymptotic solutions. *Mechanics Research Communications 31*, 3 (2004), 301–310.

[MDSB02] MEYER M., DESBRUN M., SCHRÖDER P., BARR A. H.: Discrete differential-geometry operators for triangulated 2-manifolds. In *Visualization and Mathematics III*, HEGE H.-C., POLTHIER K. (Eds.), Springer-Verlag (2002), pp. 35–57.

[MYF06] MASUDA H., YOSHIOKA Y., FURUKAWA Y.: Interactive mesh deformation using equality-constrained least squares. *Computers & Graphics 30*, 6 (2006), 936–946.

[NMK*05] NEALEN A., MÜLLER M., KEISER R., BOXERMAN E., CARLSON M.: Physically based deformable models in computer graphics. *Computer Graphics Forum 25*, 4 (2005), 809–836.

[Pai02] PAI D. K.: Strands: interactive simulation of thin solids using Cosserat models. In *Proc. Eurographics* (2002).

[PTVF02] PRESS W. H., TEUKOLSKY S. A., VETTERLING W. T., FLANNERY B. P.: *Numerical Recipes in C++: The Art of Scientific Computing*. Cambridge University Press, 2002.

[Rub00] RUBIN M. B.: *Cosserat Theories: Shells, Rods and Points*. Kluwer Academic Publisher, 2000.

[SLCO*04] SORKINE O., LIPMAN Y., COHEN-OR D., ALEXA M., RÖSSL C., SEIDEL H.-P.: Laplacian surface editing. In *Proc. Eurographics/ACM SIGGRAPH Symposium on Geometry Processing* (2004), pp. 175–184.

[Sor05] SORKINE O.: Laplacian mesh processing. In *Proc. Eurographics* (2005), pp. 53–70.

[ST07] SPILLMANN J., TESCHNER M.: CORDE: Cosserat rod elements for the dynamic simulation of one-dimensional elastic objects. In *Proc. ACM SIGGRAPH/Eurographics Symposium on Computer Animation* (2007), pp. 1–10.

[ST08] SPILLMANN J., TESCHNER M.: An adaptive contact model for the robust simulation of knots. In *Proc. Eurographics* (2008), pp. 497–506.

[TGAB08] THEETTEN A., GRISONI L., ANDRIOT C., BARSKY B.: Geometrically exact dynamic splines. *Computer-Aided Design 40*, 1 (2008), 35–48.

[TGDM07] THEETTEN A., GRISONI L., DURIEZ C., MERLHIOT X.: Quasi-dynamic splines. In *Proc. ACM Symposium on Solid and Physical Modeling* (2007), pp. 409–414.

[TKZ*05] TESCHNER M., KIMMERLE S., ZACHMANN G., HEIDELBERGER B., RAGHUPATHI L., FUHRMANN A., CANI M.-P., FAURE F., MAGNENAT-THALMANN N., STRASSER W.: Collision detection for deformable objects. *Computer Graphics Forum 24*, 1 (2005), 61–81.

[TPBF87] TERZOPOULOS D., PLATT J., BARR A., FLEISCHER. K.: Elastically deformable models. In *Proc. ACM SIGGRAPH* (1987), pp. 205–214.

[Vil98] VILLAGGIO P.: *Mathematical Models for Elastic Structures*. Cambridge University Press, 1998.

[WJZL08] WANG W., JÜTTLER B., ZHENG D., LIU Y.: Computation of rotation minimizing frames. *ACM Trans. Graph. 27*, 1 (2008), 1–18.

[WXW*06] WENG Y., XU W., WU Y., ZHOU K., GUO B.: 2D shape deformation using nonlinear least squares optimization. *The Visual Computer 22*, 9 (2006), 653–660.

Appendix A: Derivation of strain variables u_k in terms of rotation vector q

From (3) and (4), we have

$$\partial_s \mathbf{d}_k = (u_1 \mathbf{d}_1 + u_2 \mathbf{d}_2 + u_3 \mathbf{d}_3) \times \mathbf{d}_k$$
$$= u_1 \mathbf{d}_1 \times \mathbf{d}_k + u_2 \mathbf{d}_2 \times \mathbf{d}_k + u_3 \mathbf{d}_3 \times \mathbf{d}_k. \quad (39)$$

For $k = 1, 2, 3$, multiplying (39) by $\mathbf{d}_3$, $\mathbf{d}_1$ and $\mathbf{d}_2$ respectively gives:

$$u_2 = -\mathbf{d}_3 \cdot \partial_s \mathbf{d}_1, \qquad u_3 = -\mathbf{d}_1 \cdot \partial_s \mathbf{d}_2, \qquad u_1 = -\mathbf{d}_2 \cdot \partial_s \mathbf{d}_3. \quad (40)$$

Note that $\mathbf{d}_k$ is a function of $\mathbf{q}$. So,

$$\partial_s \mathbf{d}_k = \frac{\partial \mathbf{d}_k}{\partial \mathbf{q}} \cdot \partial_s \mathbf{q}. \quad (41)$$

By substituting (14) and (41) into (40), we derive:

$$u_1 = \begin{bmatrix} q_1^2 + aq_2^2 + aq_3^2 \\ cq_1q_2 + dq_3 \\ cq_1q_3 - dq_2 \end{bmatrix} \cdot \frac{\partial_s \mathbf{q}}{\|\mathbf{q}\|^2},$$

$$u_2 = \begin{bmatrix} cq_1q_2 - dq_3 \\ aq_1^2 + q_2^2 + aq_3^2 \\ cq_2q_3 + dq_1 \end{bmatrix} \cdot \frac{\partial_s \mathbf{q}}{\|\mathbf{q}\|^2}, \quad (42)$$

$$u_3 = \begin{bmatrix} cq_1q_3 + dq_2 \\ cq_2q_3 - dq_1 \\ aq_1^2 + aq_2^2 + q_3^2 \end{bmatrix} \cdot \frac{\partial_s \mathbf{q}}{\|\mathbf{q}\|^2}.$$

where a and b are as in (14), $c = 1 - a$ and $d = 1 - \cos\|\mathbf{q}\|$. Substituting (14), (15) and (42) into (10) gives the energy term expressed by the variables $\{\mathbf{r}(s), \mathbf{q}(s)\}$.